Article

Sol-Gel Synthesized Silica/Sodium Alginate Hybrids: Comprehensive Physico-Chemical and Biological Characterization

Antonio D’Angelo , Cecilia Mortalò , Lara Comune , Giuseppina Raffaini , Marika Fiorentino * , Michelina Catauro *

Posted Date: 24 July 2025

doi: 10.20944/preprints202507.2025.v1

Keywords: SiO2; Sodium alginate; sol-gel;surface area; BET; thermal analysis; moisture; cytotoxicity doi:10.20944/preprints202507.2025.v1

Article

Sol-Gel Synthesized Silica/Sodium Alginate Hybrids: Comprehensive Physico-Chemical and Biological Characterization

Antonio D'Angelo [1], Cecilia Mortalò [2], Lara Comune [3], Giuseppina Raffaini [4], Marika Fiorentino [1,*] and Michelina Catauro [1,*]

[1] Department of Engineering, University of Campania "Luigi Vanvitelli", Via Roma 29, 81031 Aversa, Italy
[2] Institute of Condensed Matter Chemistry and Technologies for Energy (ICMATE-CNR) National Research Council (CNR), C.so Stati Uniti 4, 35127 Padova, Italy
[3] Department of Environmental, Biological and Pharmaceutical Sciences and Technologies, University of Campania "Luigi Vanvitelli", Via Vivaldi 43, Caserta, 81100, Italy
[4] Department of Chemistry, Materials, and Chemical Engineering "Giulio Natta", Politecnico di Milano, Piazza L. da Vinci 32, 20131 Milan, Italy
* Correspondence: marika.fiorentino@unicampania.it (M.F.); michelina.catauro@unicampania.it (M.C.)

Abstract

The development of biomaterials with tunable properties is indispensable for advancing biomedical applications such as tissue engineering and drug delivery. In this study, amorphous silica/sodium alginate (SiO_2/SA) hybrid materials were synthesized via the sol–gel method by incorporating 2, 5, and 8% of sodium alginate into the silica matrix. The hybrids were extensively characterized to evaluate their structural, surface, thermal, moisture-responsive, and biological properties. FTIR and XRD analyses confirmed the successful formation of organic–inorganic networks and amorphous structures. BET measurements revealed a substantial increase in specific surface area for the 2 and 5% SA hybrids, reaching up to 325 m^2/g, while the 8% SA sample showed a marked decrease due to pore blocking. Moisture sorption capacity followed a similar trend. Thermal analysis indicated improved thermal behavior and partial stabilization of the polymer within the silica matrix. Cytotoxicity tests on HaCaT cells showed increased cell viability inhibition for the 2% SA hybrid, attributed to its high surface area, while the 5 and 8% hybrids showed better biocompatibility. Overall, the SiO_2/SA 5% hybrid demonstrated the best balance between enhanced functional properties and a good biocompatibility, suggesting it as the most promising candidate for future biomedical applications.

Keywords: SiO_2; sodium alginate; sol-gel; surface area; BET; thermal analysis; moisture; cytotoxicity

1. Introduction

Biomaterials are a class of materials able to interact with specific part of the human body to enhance and assist tissue regeneration. Indeed, their interaction with damaged tissues stimulate growth and repair [1–3]. Nowadays, several biomaterials, including natural and synthetic polymers, metal oxides, and bioceramics, provide flexible solutions for tissue regeneration and drug delivery. According to their composition, they are divided into four categories: i) metallic, ii) ceramic, iii) polymers and iv) biocomposites [4,5]. Among ceramics, amorphous silica represents a valuable choice as a biomaterial due to its chemical inertness, which prevents undesirable reactions with surrounding molecules. Moreover, it exhibits favourable surface properties, such as a well-developed surface area and numerous hydroxyl groups on its surface. Unlike bioceramics obtaining through traditional melting process, sol–gel-derived glasses are produced at lower temperatures, resulting in higher surface area and porosity [6–8]. This improves bioactivity [9], bone bonding [10,11], drug release [12], and degradation rates [13].

The abundance of –OH groups on the silica surface enables hydrogen bonding with various pharmacologically relevant molecules, which can be adsorbed onto its porous structure, making it highly suitable for drug delivery applications [14]. In addition, the high surface area of amorphous silica contributes to its biomimetic potential and biocompatibility [15]. The rough surface topography also facilitates cell attachment and proliferation of stem cells, which play a key role in effective tissue regeneration, and promote better integration with biological tissues [16,17].

The incorporation of a natural organic polymer into the silica matrix improves the biocompatibility and increases the tolerance within the host tissue. It also enhances degradability of the material, potentially eliminating the need for a further surgical procedure to remove the material once the tissues have healed and regenerated [18,19].

Numerous studies have highlighted that incorporating natural polymer into the inorganic silica matrix can significantly improve the properties of silica-based biomaterials. For instance, the combination of chitosan with silica to form xerogels has been shown to exhibit a high surface area, bioactivity and osteoconductive properties, thereby enhancing cell differentiation and prompting quick bioactive responses [20]. Similarly, the silica/collagen system synthesized via the sol-gel provided a fiber-reinforced, porous structure with mechanical properties applicable to bone proliferation for in low-load-bearing areas of body [21]. Other hybrids have been synthesized by combining silk fibroin with silica, improving their biomedical applicability [22]. Another organic polymer of biomedical interest is alginate, a polysaccharides obtained from cell walls of brown algae and bacterial capsule of *Azotobacter* sp. and *Pseudomonas* sp. The most common form is sodium alginate [23].

Alginates are composed of alternating β-D-mannuronic acid (M) and α-L-guluronic acid (G) units, which are linked by 1,4-glycosidic bonds. Alginates with a high M content form more elastic, non-toxic, and non-immunogenic hydrogels, making them more biocompatible, more degradable, and highly suitable for soft tissue regeneration and controlled drug release [18,24]. The incorporation of this biopolymer increases the biocompatibility of silica-based biomaterials and improves their structural properties, particularly the swelling capacity, allowing them to absorb of body fluids without structural collapse, thereby increasing their adaptability within human tissues [18,25–27].

Since most of the literature finding deals with hybrid materials in which silica nanoparticles are embedded in alginates beads or composites [28,29], the aim of this work is to synthesize SiO_2/sodium alginate (SA) hybrid materials by incorporating 2, 5, and 8% of the polymer via the sol-gel route, to obtain biomaterials with enhanced properties for potential applications in the biomedical field. The hybrids were characterized in terms of their chemical composition using FTIR, structural features through XRD analysis, surface area via BET analysis, as well as their thermal behavior and moisture sorption capacity. Biocompatibility was assessed by testing the hybrids against HaCaT cell cultures, which are used as a model of healthy human cells. The goal was to obtain preliminary data to evaluate how the incorporation of sodium alginate can improve the properties of amorphous SiO_2. Since most of the literature finding deals with hybrid materials in which silica nanoparticles are embedded in alginates beads or composites [28,29], the aim of this work is to synthesize SiO_2/sodium alginate (SA) hybrid materials by incorporating 2, 5, and 8% of the polymer via the sol-gel route, to obtain biomaterials with enhanced properties for potential applications in the biomedical field. The hybrids were characterized in terms of their chemical composition using FTIR, structural features through XRD analysis, surface area via BET analysis, as well as their thermal behavior and moisture sorption capacity. Biocompatibility was assessed by testing the hybrids against HaCaT cell cultures, which are used as a model of healthy human cells. The goal was to obtain preliminary data to evaluate how the incorporation of sodium alginate can improve the properties of amorphous SiO_2.

2. Results and Discussion

2.1. Sol-Gel Synthesis

The SiO_2/SA hybrids, as well as the pure SiO_2, were synthesized using the sol-gel technique through hydrolysis and polycondensation reactions in the presence of water and ethanol. The synthesis was conducted under acidic conditions to accelerate the hydrolysis reactions relative to the condensation steps. The acidic environment promotes the hydrolysis of the tetraethyl orthosilicate (TEOS) precursor by facilitating the cleavage of alkoxy (–OR) groups from the water molecules and leads to the formation of numerous silanol (–Si–OH) groups. The subsequent delay in the condensation of these silanol groups, caused by the protonation of the hydroxyl moieties, results in the formation of a limited number of nuclei. These nuclei then grow into large amorphous silica bulks, characterized by a dense matrix with a fine and narrowly distributed porosity [30]. The incorporation of sodium alginate (SA) significantly modifies this process. Under acidic conditions, the carboxylate groups ($–COO^-$) of SA are protonated to –COOH, losing their negative charge and becoming capable of forming hydrogen bonds with the silanol groups (–Si–OH) generated from TEOS hydrolysis, the SiO_2 precursor of these sol-gel synthesis [23]. These hydrogen bonds promote the formation of an organic–inorganic hybrid network and locally inhibit or modulate the condensation of the silica species. Additionally, SA adopts a highly hydrated and expanded conformation in aqueous solution due to its polyelectrolyte nature. During the early stages of silica condensation, this polymer network swells, taking up space and sterically hindering the formation of compact silica agglomerates [31]. As a result, preliminary morphological observations based on the acquired digital photographs of dried SiO_2/SA hybrids showed spongy-like structures, potentially indicating a more open porosity respect to pure SiO_2. In addition, hybrids lost the typical transparency of SiO_2 glass appearing instead of opaque and white materials (Figure 1).

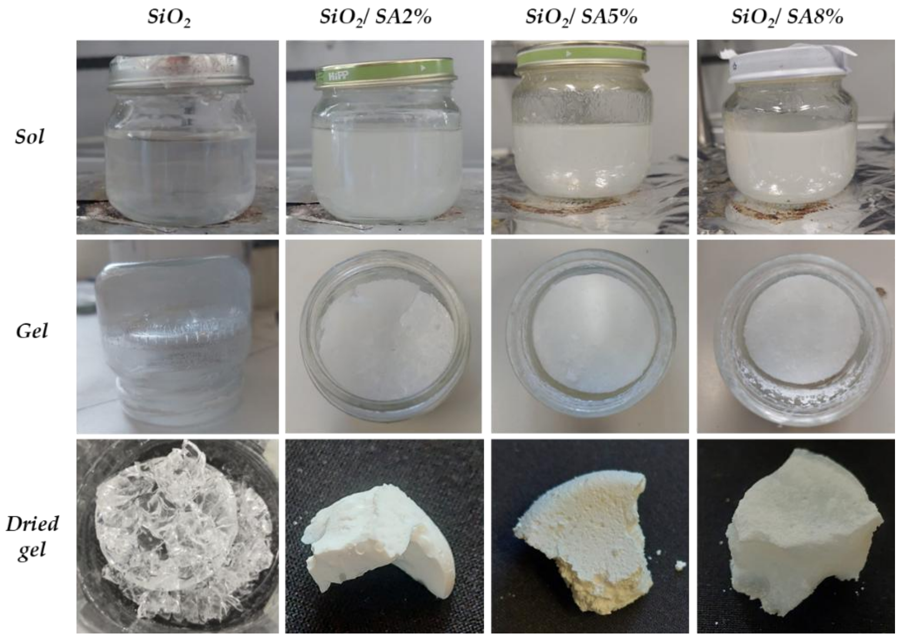

Figure 1. SiO_2/SA hybrids images compared to SiO_2 in sol, gel, dried gel steps.

2.2. FTIR Analysis

An FTIR study was performed to investigate the interaction between the SiO_2 network and sodium alginate (SA) polymer during formation of the hybrid materials. The FTIR spectra of SiO_2/SA hybrids, pure SiO_2, and pure SA are shown in Figure 2. In the spectrum of pure sodium alginate, the broad band centered at 3443 cm^{-1} is attributed to O–H stretching vibrations of hydroxyl groups while the sharp peaks at 2926 cm^{-1} and 2852 cm^{-1} correspond to the C–H stretching vibrations of methylene

(–CH₂–) groups in the saccharide backbone [32,33]. The peaks at 1628 cm⁻¹ and 1418 cm⁻¹ are assigned to the asymmetric and the symmetric stretching vibrations of carboxylate (νCOO⁻) groups, respectively [34,35]. The band at 1308 cm⁻¹ is attributed to C–O stretching. Meanwhile, the peaks at 1086 cm⁻¹ and 1040 cm⁻¹ are associated with νC–O and νC–O–C stretching modes, linked to mannuronic (M) and guluronic (G) units [36,37]. These features, particularly the C–H stretching and symmetric νCOO⁻ peaks, are still visible in the spectra of hybrid samples and increase in intensity with SA content (as indicated by pink arrows in Figure 2). In pure SiO_2, the broad band centered at 3455 cm⁻¹ and the peak at 1641 cm⁻¹ are attributed to O–H stretching and bending vibrations, respectively, from silanol groups. The 1641 cm⁻¹ band undergoes a red shift to 1637 cm⁻¹ in the SiO_2/SA 8% hybrid, suggesting the formation of hydrogen bond between silanol groups and polysaccharide hydroxyls [38,39] The broad band at 1079 cm⁻¹ and the peak at 796 cm⁻¹ in pure silica correspond to Si–O–Si asymmetric and symmetric stretching vibrations, respectively [40]. The 796 cm⁻¹ band shows a gradual red shift with increasing SA, reaching 791 cm⁻¹ in the 8% hybrid, indicating a weakening of the siloxane network due to hydrogen bonding between alginate –COOH groups and bridging oxygen atoms in silica. Conversely, the Si–O–Si asymmetric band shifts towards higher wavenumbers (i.e., a blue shift), reaching ~1096 cm⁻¹ in the 8% SA hybrid. Additionally, its shape changes significantly, suggesting overlapping contributions from both Si–O–Si vibrations and carboxylate bands at ~1068 and 1040 cm⁻¹. The increasing intensity and complexity of this band may also be due to the growing presence of –COO⁻ groups from SA overlapping the Si–O–Si signal.

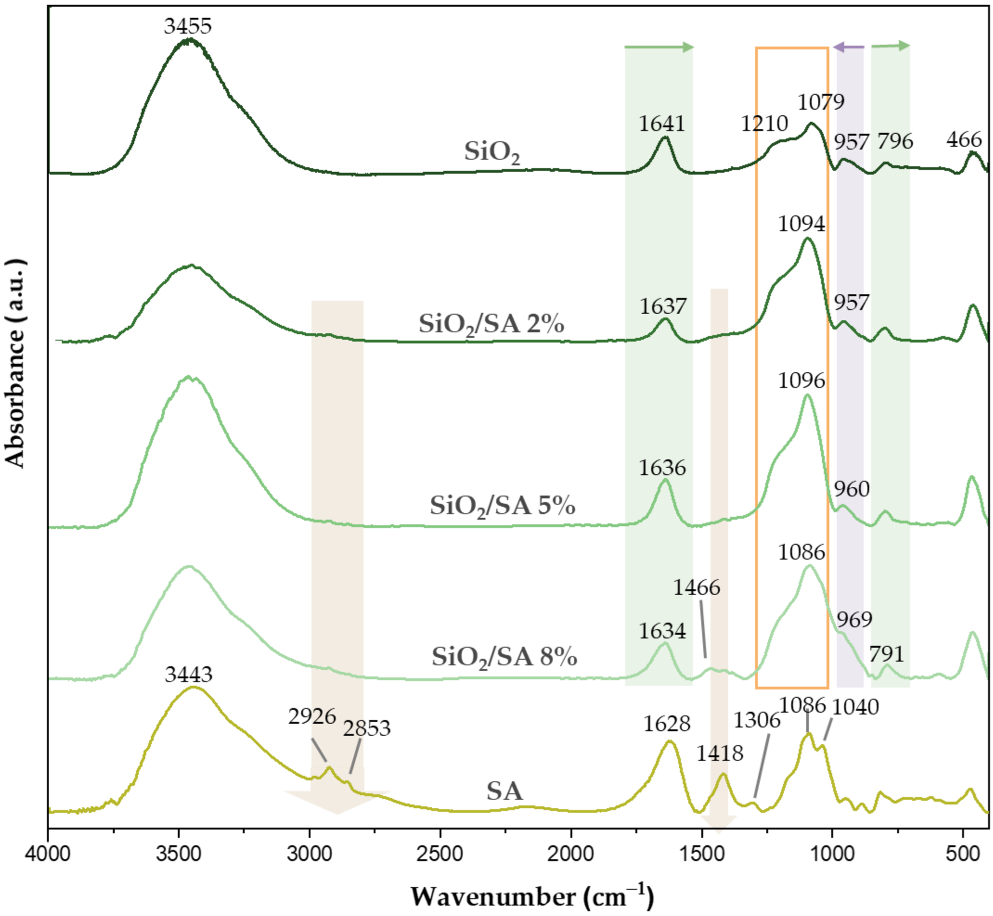

Figure 2. FTIR spectra of SiO_2/SA hybrids. Pink arrows indicate increasing peak intensity; green filled squares indicate red shifts; violet filled squares indicate blue shifts; orange empty squares highlight the complex Si–O–Si band region.

To further investigate the impact of the polymer on the silica network peak deconvolution was performed in the 1600–800 cm⁻¹ region of the Si-O-Si stretching band. Pure SiO_2 displays seven deconvoluted peaks at approximately 1252, 1210, 1137, 1077, 1035, 963, and 932 cm⁻¹, which attributed to the asymmetric stretching modes of the transverse optical (TO) siloxane framework [41]. According to De los Arcos et al., the peaks at 1137 and 1210 cm⁻¹ (both associated with TO–AS_2 modes) reflect different structural features: the 1137 cm⁻¹ band is directly related to terminal silanol groups (Si–OH) which are present on the surface or within porous domains, indicating reactive sites and surface defects. The 1210 cm⁻¹ peak corresponds to asymmetric Si–O–Si vibrations and is typically used as a marker of topological disorder and reduced network connectivity. The bands in the 1035–1077 cm⁻¹ region (TO–AS_1) are attributed to more ordered and crosslinked Si–O–Si domains, while the lower-frequency peaks at 963 and 932 cm⁻¹ are associated with silanol bending and stretching modes, further indicating structural defects and surface hydroxylation [41]. SA exhibits characteristic saccharide bands that partially overlap with the Si–O–Si stretching region: 1154 and 1112 cm⁻¹ (asymmetric and symmetric C–O–C stretching), 1085 and 1041 cm⁻¹ (C–O and C–O–C vibrations from mannuronic/guluronic units), and 947 and 888 cm⁻¹ in the anomeric region, associated with glycosidic bond vibrations and deformation modes [42]. The deconvolution analysis of the SiO_2/SA hybrids reveal significant spectral modifications, indicating molecular interactions and structural rearrangements (Figure 3). The 1137 cm⁻¹ band (grey curve in Figure 3) which is associated with terminal Si–OH groups in pure SiO_2 disappears in the hybrid samples, suggesting a chemical interaction with the –COOH groups of sodium alginate. Additionally, the 1210 cm⁻¹ band (green curve in Figure 3) is red shifted to approximately 1191 cm⁻¹ upon hybrid formation, accompanied by increased intensity. This shift indicates enhanced structural disorder induced by SA incorporation. The area of the TO–AS_2 band (initially centered at 1210 cm⁻¹) increases with increasing SA content, reaching a maximum in the SiO_2/SA 5% sample, and decreasing slightly at 8%. This is likely due to a redistribution of vibrational modes and the growing influence of the organic phase. The 1085 cm⁻¹ band (yellow curve in Figure 3) also shows increased intensity with higher SA content, due to overlapping contributions from the 1077 cm⁻¹ SiO_2 band and the 1085 cm⁻¹ saccharide band of SA. This TO–AS_1 contribution increases from 15 to 68 of the total area (Figure 4) due mainly to SA increasing amount. Finally, the 963 cm⁻¹ band (red curve in Figure 3) increases significantly in intensity in the hybrid materials and correlates with the SA concentration. Its integrated area increases fourfold compared to pure SiO_2, further confirming the incorporation of organic content (Figure 3). Although primarily associated with Si–OH bending vibration, this band likely includes growing contributions from from glycosidic bonds and suggests that the alginate structure remains intact despite acidic conditions. This indicates a protective effect of the silica matrix, which likely shields the polymer from acid hydrolysis during hybrid formation [23].

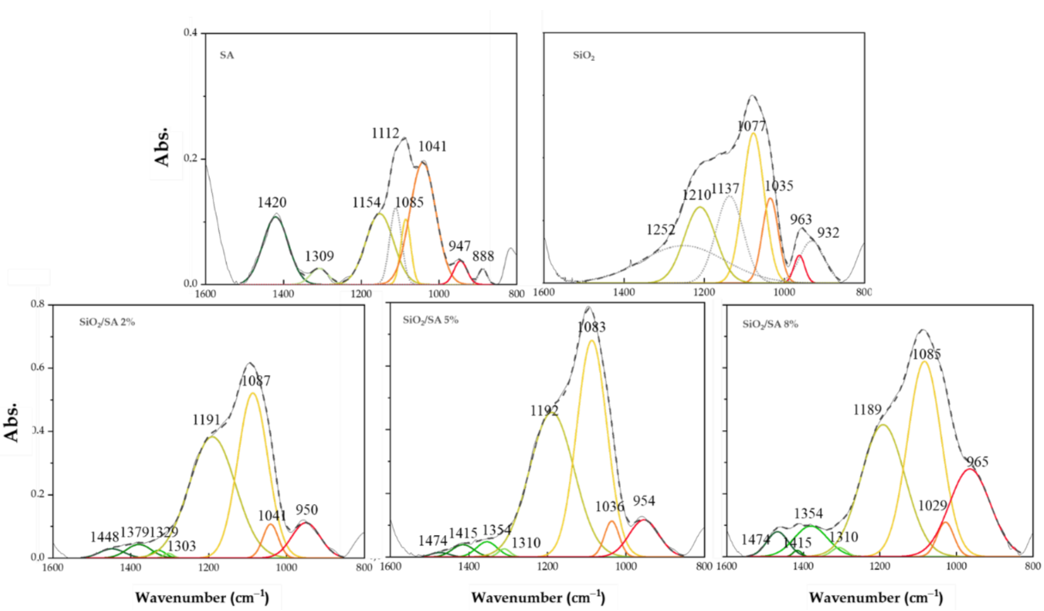

Figure 3. Deconvoluted spectra of SiO_2/SA hybrids in the range of 1600-800 cm⁻¹ compared to pure SiO_2.

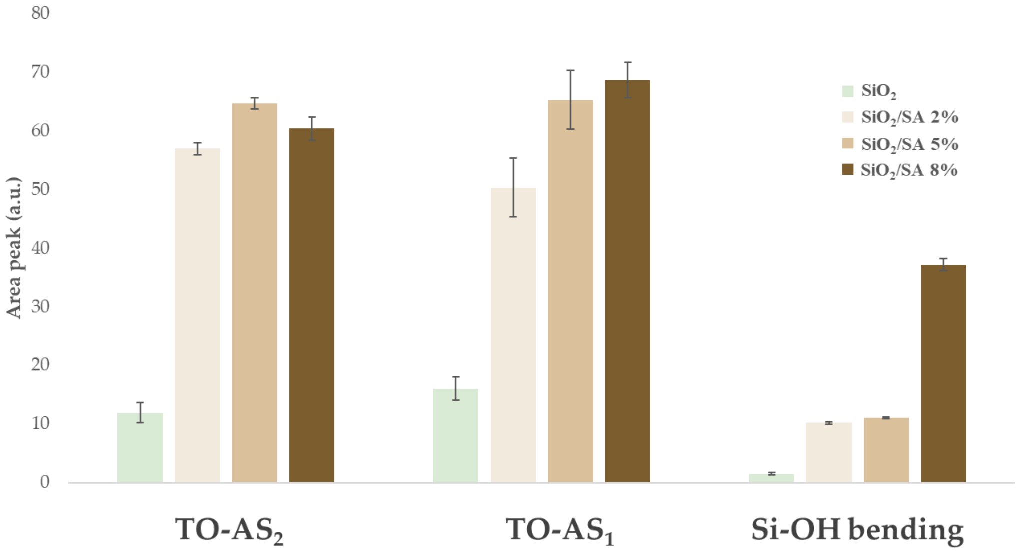

Figure 4. Area peak of deconvoluted Si-O-Si band in the range 1600-800 cm^{-1} of SiO_2/SA hybrids in the range of 1600-800 cm^{-1} compared to SiO_2. TO-AS$_2$: 1210 cm^{-1} peak; TO-AS$_1$: 1077-1085 cm^{-1} peak.

2.3. XRD Analysis

Figure 5 shows XRD spectra of pure SA and SiO_2, as well as the SA/SiO_2 hybrids materials prepared by the sol-gel method. The diffractogram of the sodium alginate sample (Figure 5(a)) exhibits two broad signals centered at 13.6, 21.8°. These peaks are attributed to the (1 1 0) and (2 0 0) planes of the guluronate (G) and mannuronate (M) units, respectively [43–45]. The additional peak at 24° is also attributable to the sodium alginate structure as observed in some recent works [46,47]. The XRD patterns of the SiO_2/SA hybrids (Figure 5(c–e)) showed amorphous structures, similar to pure SiO_2 (Figure 5(b)). A broad peak around 23° indicates low crystallinity. The crystalline signals of sodium alginate disappeared into the broad SiO_2 peak, suggesting that the polymer is present either in an amorphous state or as very small crystallites undetectable by XRD. This result is consistent with other SiO_2-based hybrid materials prepared by the sol-gel method, where crystalline organic polymers or drugs were incorporated, as reported in other studies [48,49].

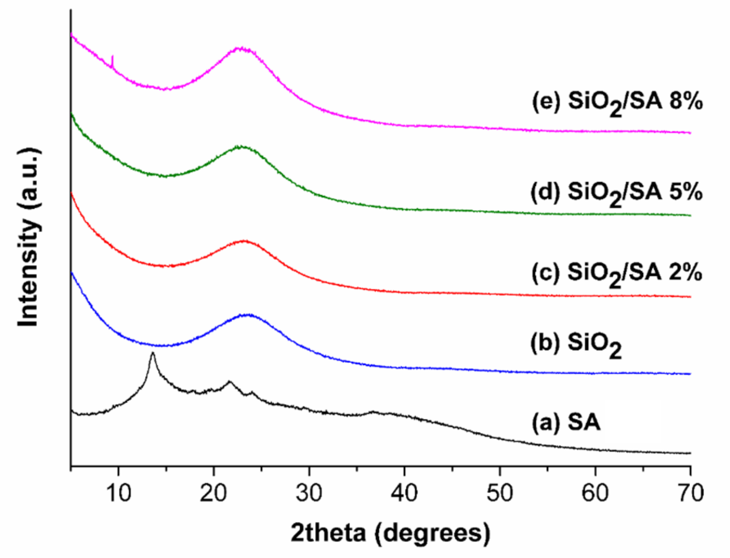

Figure 5. XRD profiles of pure SA and SiO_2 and SiO_2/SA hybrids materials prepared by sol-gel method.

2.4. BET Study

Table 1 reports the specific surface area values determined by the Brunauer-Emmett-Teller (BET) method for samples pre-treated at 80 °C for 24 hours. The BET analysis involves the adsorption of nitrogen gas onto the sample surface at low temperatures. The gas molecules form a monomolecular layer, and by knowing the diameter of the nitrogen molecule and the number of molecules required for complete coverage, the total surface area of the sample can be calculated. As shown in Table 1, the specific surface area of the as received SA is very low (0.2307 m^2/g), which is consistent with its semicrystalline nature observed in the XRD analyses. In contrast, the bare SiO_2 gel exhibits a significantly higher surface area value (9.6861 m^2/g), typical of its amorphous structure. Interestingly, a synergistic effect between SA and SiO_2 is observed: the specific surface area of the SiO_2/SA hybrid gels increases by more than one order of magnitude compared to pure SiO_2. The highest BET surface area (325.2 m^2/g) is recorded for the SiO_2/SA 2% sample, while the surface area decreases to 138.7 and 104.3 m^2/g in hybrids containing 5 and 8% SA, respectively. The initial increase in surface area with the addition of a small amount of SA (2%) can be attributed to the highly hydrated and expanded conformation of alginate in aqueous solution, which forms a swollen polymer network as previously discussed in paragraph 2.1. The weak interaction between the alginate and the silica matrix prevents shrinkage or structural collapse during gelation and drying promoting the formation of a more open structure with a greater accessible surface area. However, at higher SA content (5 and 8%), the surface area decreases by approximately two-fold and three-fold, respectively. This can be explained by the increasing of SA filling the voids within the silica network, reducing the accessible surface, and altering the hybrid gel structure. These results are in good agreement with those reported by Han et al. for sodium alginate-silica composite aerogels prepared using the sol-gel process followed by freezing drying [50]. In their study, it was observed that increasing the sodium alginate content led to a gradual thickening of the composite aerogel cell walls, hindering pore formation and decreasing pore volume.

Table 1. BET Surface Area on all prepared samples after treatment at 80 °C for 24 hours.

Samples	BET Surface Area (m^2/g)
SA	0.2307 ± 0.0067
SiO_2	9.6861 ± 0.3576
SiO_2 / SA 2%	325.2401 ± 5.3292
SiO_2 / SA 5%	138.6862 ± 2.1163
SiO_2 / SA 8%	104.3471 .0956

2.5. Moisture Sorption Analysis

A moisture absorption test was conducted on the hybrid materials to evaluate the effect of incorporating SA the moisture sorption capacity of SiO_2, wich is well known for their hydrophilicity due to large number of hydroxyl groups on its surface [51]. This property is particularly relevant for biomaterials designed for cell and tissue contact, as the ability to retain moisture improves biocompatibility, supports cell viability, and facilitates integration within hydrated biological environments [52]. The moisture sorption graphs show the ratio of the weight at various time points to the initial weight of different samples exposed to 99% relative humidity, reflecting their moisture uptake behaviour (Figure 6). Pure SiO_2 exhibits relatively limited moisture absorption, reaching a weight ratio of approximately 1.23 after 72 hours. Conversely, pure sodium alginate (SA) exhibits significantly higher moisture uptake, reaching a weight ratio close to 1.73. SiO_2/SA hybrid materials display intermediate moisture absorption characteristics: higher than pure SiO_2 but generally lower than pure SA. Notably, the hybrids containing 2% and 5% SA demonstrate the highest moisture uptake, approaching a weight ratio of 1.9 at 72 hours. In contrast, the 8% SA hybrid absorbs less moisture relative to these two but more than pure SiO_2. These observations correlate strongly with the BET-specific surface area measurements. The hybrids with 2% and 5% SA possess substantially increased surface areas (approximately 325 m²/g and 139 m²/g, respectively) compared to pure SiO_2 (≈9.7 m²/g) and pure SA (≈0.23 m²/g). This indicates enhanced mesoporosity and a greater available surface for interaction with water molecules, facilitating higher moisture uptake. The reduced moisture absorption of the 8% SA hybrid aligns with its lower surface area compared to the 2% and 5% hybrids, suggesting that the increased SA content begins to fill the open pores of the hybrid matrix, thereby reducing the availability of sites for moisture uptake.

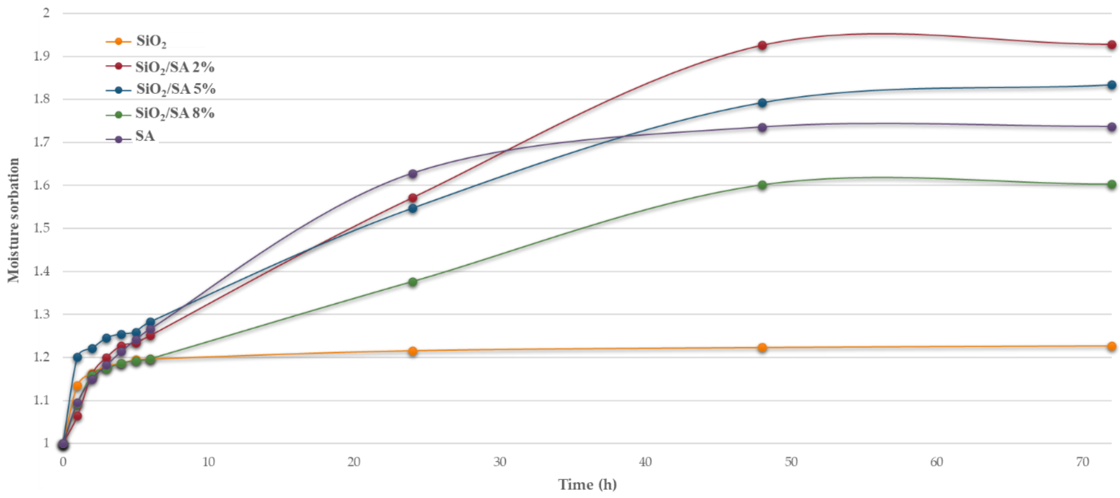

Figure 6. Moisture absorption test of SiO_2/SA hybrids underwent 99% relative humidity.

2.5. Thermal Analysis

Thermal analysis was carried out to assess the thermal stability of sodium alginate (SA) within the SiO_2/SA hybrid materials under nitrogen atmosphere. The TGA/DSC curve of pure SA (Figure 7) shows four main mass loss events. The first stage, from 200 °C to 350 °C shows a further mass loss of about 40.34%, associated with the thermal decarboxylation of uronic acid residues [53] and cleavage of the glycosidic backbone [54–56]. This is accompanied by an endothermic peak in the DSC curve. In the second stage (350–500 °C), a further 13.40% mass loss, attributed to carbonization of the polymer matrix and the formation of sodium carbonate (Na_2CO_3). Finally, between 550 °C and 900 °C, a further 30.81% mass loss is observed due to the decomposition of Na_2CO_3 into sodium oxide (Na_2O) and CO_2, as confirmed by the DTG peak at 786.78 °C [57–59].

The TGA (Figure 8A) and DTG (Figure 8B) curves of the SiO_2/SA hybrids show altered thermal degradation behaviour compared to pure SA. The decarboxylation process remains largely unaffected by the silica matrix, as evidenced by the similar positions of the DTG peak (~223–237 %/°C) for all hybrid samples. However, the 8% SA hybrid exhibits a slightly higher DTG peak (237.36 %/°C), suggesting enhanced thermal stability. This stabilization can be interpreted in the context of the reduced surface area of this sample (104.35 m²/g), compared to higher values observed for SiO_2/SA 2% (325.24 m²/g) and SiO_2/SA 5% (138.69 m²/g). The lower surface area likely limits the exposure of the polymeric fraction to thermal flow, thus slowing degradation. Across all hybrids, the total mass loss is significantly reduced compared to pure SA, consistent with the lower polymer content. The carbonization step (350–500 °C) is still evident, with mass losses increasing with SA content: 4.21%, 6.86%, and 6.93% for SiO_2/SA 2%, 5%, and 8%, respectively. This trend reflects a more extensive carbonization process in hybrids with higher organic content. Notably, the Na_2CO_3 decomposition step observed in pure SA (550–860 °C) is completely absent in the hybrids, as indicated by the lack of a DTG peak in this range [60]. This suggests a reduced presence of residual sodium species or their encapsulation within the silica matrix, which may inhibit their thermal decomposition under inert conditions. A summary of the main thermal events for pure SA and the hybrid materials is reported in Table 2.

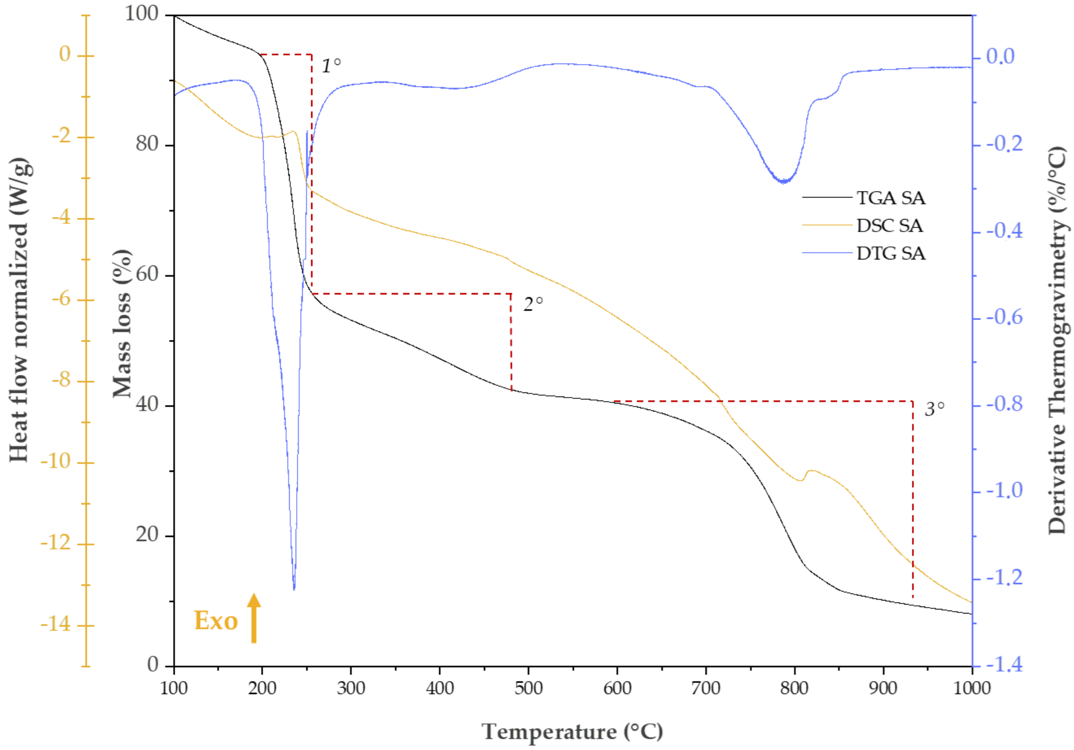

Figure 7. TGA, DSC and DTG curves of pure sodium alginate. Mass loss of TGA curves is underlined with red dashed curve.

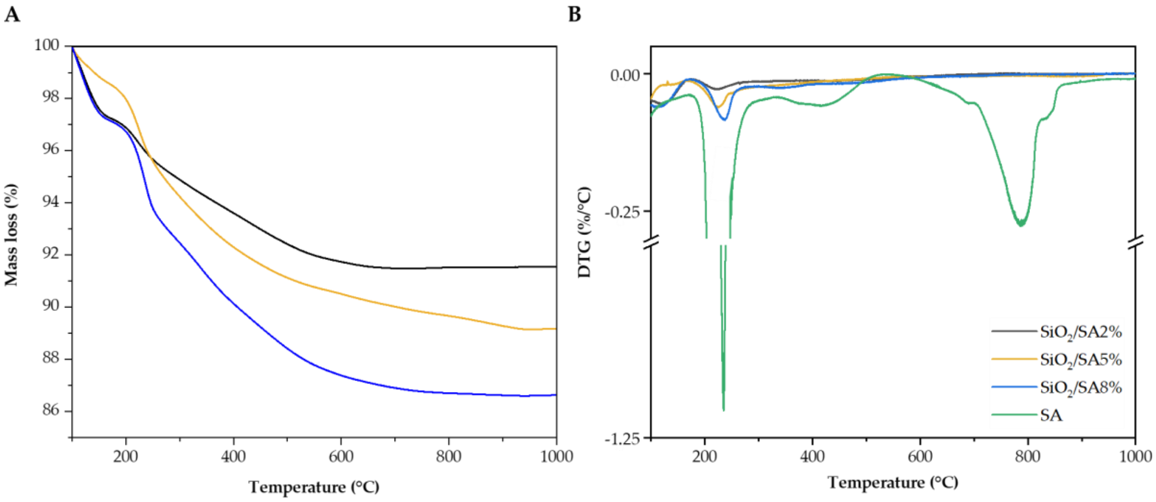

Figure 8. (A) TGA curves of SiO_2/SA hybrids; (B) DTG curves of SiO_2/SA hybrids compared to pure SA.

Table 2. Summary table of SiO_2/SA hybrids and SA thermal events, mass loss and DTG values.

		Mass loss (%) / DTG (%/°C)			
T_{range}/°C	Phenomena	SA	SiO_2/SA2%	SiO_2/SA5%	SiO_2/SA8%
200 – 250	1. Decarboxylation (Exo)	40.34%, 234.78 %/°C	1.82% 223.01%/°C	3.57% 224.91 %/°C	3.61% 237.36 %/°C
350 – 500	2. Na_2CO_3 formation (Exo)	13.40% 417.37%/°C	4.21%	6.86%	6.93%

550 – 860	3. Na_2CO_3 decomposition (Endo)	30.81% 786.78%/°C	-	-	-

2.6. Cytotoxicity Study

A cytotoxicity assessment was conducted using HaCaT cells, an established model of healthy human keratinocytes, to evaluate the biocompatibility of hybrid SiO_2/SA materials in comparison with their individual components, pure SiO_2 and pure sodium alginate (SA) (Figure 9). Both references exhibited low cytotoxicity, with cell viability inhibition (CVI%) values remaining below 20%. Interestingly, incorporation of 2% SA into the silica matrix (SiO_2/SA 2%) led to a marked increase in cytotoxicity, elevating CVI% to approximately 40%. This trend was reversed at higher SA loadings: SiO_2/SA 5% showed a CVI% of about 33%, and SiO_2/SA 8% returned to values comparable to pure SiO_2, around 15%. These results suggest that the cytotoxicity of the hybrids is not simply governed by the presence of SA, known to be biocompatible, but rather by the physicochemical changes introduced upon hybrid formation. BET analysis revealed that SiO_2/SA 2% possessed a specific surface area nearly three times greater than that of pure SiO_2, which may account for the enhanced interaction with cell membranes and the observed cytotoxicity. As the SA content increased, the surface area decreased accordingly, paralleling the drop in cytotoxic effects. This is also because of the anti-inflammatory effect of SA [61]. Furthermore, these findings are consistent with previous literature showing that an increased surface area in nanostructured materials can amplify cell-material interactions, leading to higher biological reactivity. As demonstrated by Spyrogianni et al. (2017), both particle size and surface area are critical determinants of silica nanoparticle cytotoxicity [62]. Overall, the data indicate that tuning the SA content in SiO_2-based hybrids allows modulation of cytotoxicity, with intermediate compositions (e.g., 2–5%) requiring careful evaluation due to their heightened surface reactivity.

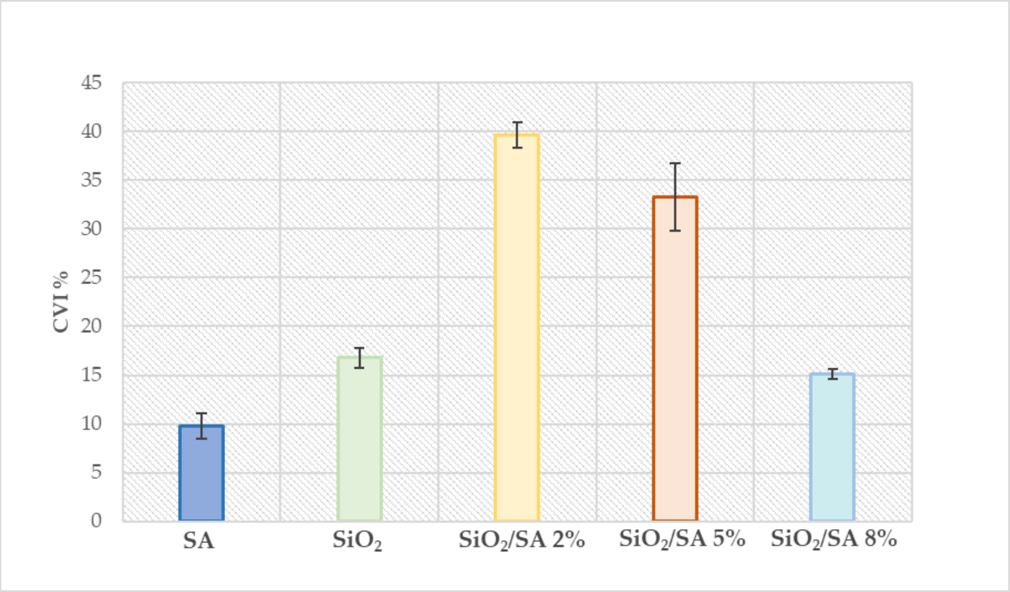

Figure 9. Cell viability inhibition of SiO_2/SA hybrids against HaCaT cell line. CVI:Cell Viability Inhibition.

3. Materials and Methods

3.1. Sol-Gel Synthesis

SiO_2 and SiO_2/SA hybrid materials containing 2, 5, and 8% of SA were synthesized via a sol–gel route. SA was purchased from Thermo Fisher Scientific (Waltham, MA, USA; Product number A18565, Lot 10242904), characterized by a low viscosity of 9 mPa·s (1% solution at 20 °C). The required amounts of SA, corresponding to 2, 5, or 8% by weight relative to the final SiO_2 mass, were dissolved in deionized water and slowly added to the solution in a beaker placed on a magnetic stirrer at 40 °C. For the pure SiO_2 sample, no SA was added. Tetraethyl orthosilicate (TEOS, $Si(OC_2H_5)_4$, Sigma-Aldrich, St. Louis, MO, USA) was used as the silica precursor and dissolved in methanol (≥99.8%, HiPerSolv CHROMANORM®, gradient grade for HPLC, VWR; purchased from Sigma-Aldrich), which served as a co-solvent. Hydrochloric acid (HCl, 37% w/w, CAS No. 7647-01-0, MFCD00011324) was obtained from Sigma-Aldrich Fine Chemicals Biosciences (Product code H1758100ML, 100 mL). The SA solution was added dropwise to the TEOS/methanol mixture to obtain a stable, white, opalescent mixture free of visible aggregates or phase separation. The molar ratios employed for all samples were: TEOS:SiO_2 = 1; H_2O:TEOS = 10.1; MeOH:TEOS = 3.8. The final sol was stirred at room temperature for 5 hours. After stirring, the system was sealed to allow gelation. The resulting gels were dried in a static oven at 50 °C until complete solvent removal. The dried materials were then stored in airtight containers for further characterization.

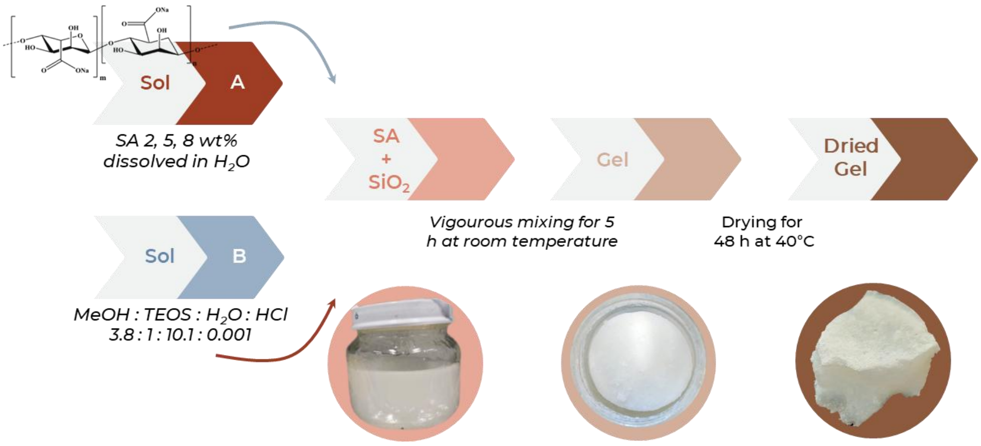

Figure 10. Sol-gel synthesis of SiO_2/SA hybrids. SA: Sodium alginate; TEOS: Tetraethyl orthosilicate; MeOH: Methanol.

3.2. FTIR Analysis

FTIR spectra was recorded using the Prestige21 Shimadzu system, equipping a DTGS KBr detector. A resolution of 2 cm^{-1} was used, and 60 scans were acquired within the range of 400–4000 cm^{-1}. 1:100 = sample:KBr disks were prepared for analysis. FTIR spectra were elaborated using IRsolution (version 1.60, Shimadzu, Milan, Italy) and Origin 8 (version 2022b, OriginLab Corporation, Northampton, MA, USA) softwares. The spectra of pure silica and pure sodium alginate were used as comparisons.

3.3. XRD Analysis

A Philips X'Pert PRO diffractometer (now part of Malvern PANAlytical, Malvern, UK) equipped with a fast detector (X'Celerator) was used for the XRD investigations. Measurements were carried out at room temperature with continuous sweep, using Cu-kα radiation (λ = 1.5405 Å), with a voltage of 40 kV and a current of 40 mA, in the 2θ range from 5 to 70° with a step of 0.04° and a time per step of 500 sec.

3.4. BET Study

The surface area was determined by BET analysis (Micromeritics GEMINI V, Norcross, Georgia, USA). The samples were previously heated to a sufficiently high temperature, using nitrogen cleaning gas, to favor the evaporation of any pollutant substances present on the surface of the particles but such as not to modify the value of the total surface of the grains, in order to not to hinder or distort the absorption of the measuring gas.

3.5. Moisture Absorption Analysis

The hybrid SiO_2/SA, SiO_2, and SA samples were first ground and then dried under vacuum for 24 hours to completely remove any residual moisture. Each sample was then individually placed inside a vacuum chamber maintained at a controlled relative humidity of 99%, using a thermostat-regulated system. The sample weight was recorded at regular intervals: every hour for the first 8 hours, and subsequently at 24 and 48 hours. The experiment was carried out separately for each sample to avoid interactions between materials and to ensure consistent humidity conditions within the chamber.

3.6. Thermal Analysis

The thermal analysis of SiO_2/SA hybrids was studied through simultaneous DSC/TGA with the Discovery SDT 650. The materials were grounded before starting the analysis. Approximately 10 mg of each sample was placed in a 90 µL alumina crucible. The flow rate applied for the test was 100 mL/min with a heating rate of 5 °C/min, starting from 100°C to 1000°C in both hybrids and references (SA and SiO_2) as reported in Fiorentino et al. 2024 [63]. Measurements were elaborated using TRIOS software by TA Instruments and Origin 8 software.

3.7. Cytotoxicity Study

Human keratinocyte cell line (HaCaT) was cultured at 37 °C in a humidified incubator with 5% CO_2, using Dulbecco's Modified Eagle Medium (DMEM) supplemented with 10% fetal bovine serum, 50 U/mL penicillin, and 100 µg/mL streptomycin [64]. Cells were seeded into 96-well plates at a density of 2.0×10^4 cells per well and exposed to 1 mg of the test materials for 24 hours [65]. Cell viability inhibition (CVI%) was evaluated using the MTT assay, which measures mitochondrial dehydrogenase activity, serving as an indirect indicator of potential cytotoxic effects through changes in cellular metabolic activity. Each experimental condition was tested in triplicate in independent assays. Data are reported as mean ± standard deviation.

5. Conclusions

The study demonstrated how the incorporation of different percentages of sodium alginate (SA) into the amorphous silica (SiO_2) matrix via sol-gel synthesis significantly alters the physico-chemical and biological properties of the resulting hybrid materials. BET and moisture absorption analyses revealed a significant increase in specific surface area and absorption capacity of the samples containing 2 and 5% SA. This was attributed to the more open and porous structure induced by the polymer network. However, the increased surface area in the 2% hybrid led to higher cytotoxicity toward HaCaT cells, presumably due to greater interaction with cell membranes. In contrast, the hybrid with 8% SA exhibited the best biocompatibility, albeit with surface area, likely due to the polymer filling effect. Taking into account the balance between physico-chemical performance and biological response, the SiO_2/SA 5% hybrid offers the best compromise, providing good specific surface area and absorption capacity, as well as and reasonable cell compatibility. Therefore, It is hypothesized that this material is the most promising candidate for biomedical applications, such as controlled drug delivery or tissue regeneration.

Author Contributions: Conceptualization, M.C. and M.F.; methodology, M.F., A.D., C.M., L.C.; software, M.F., G.R.; validation, M.F. and C.M., formal analysis, M.F., A.D., C.M.; investigation, M.F., A.D., C.M., L.C.; resources, M.C., C.M., data curation, M.F.; writing—original draft preparation, M.F., A.D., C.M.; writing—review and editing, All; visualization, M.F. and A.D.; supervision, M.C.; project administration, M.C.; funding acquisition, M.C.. All authors have read and agreed to the published version of the manuscript.

Funding: This research received no external funding

Institutional Review Board Statement: Not applicable.

Informed Consent Statement: Not applicable.

Data Availability Statement: The original contributions presented in this study are included in the article. Further inquiries can be directed to the corresponding author(s).

Acknowledgments: The authors have reviewed and edited the output and take full responsibility for the content of this publication.

Conflicts of Interest: The authors declare no conflicts of interest.

References

1. Langer, R.; Vacanti, J.P. Tissue Engineering. *Science* **1993**, *260*, 920–926, doi:10.1126/science.8493529.
2. He, X.; Han, Z.; Ruan, Y.; Wang, Z.; Liao, B.; Li, X.; Tan, J.; Han, X.; Shen, J.; Bai, D. Smart Responsive Biomaterials for Spatiotemporal Modulation of Functional Tissue Repair. *Materials Today Bio* **2025**, *33*, 102063, doi:10.1016/j.mtbio.2025.102063.
3. Baskaran, P.; Muthiah, B.; Uthirapathy, V. A Systematic Review on Biomaterials and Their Recent Progress in Biomedical Applications: Bone Tissue Engineering. *Reviews in Inorganic Chemistry* **2025**, doi:10.1515/revic-2024-0062.
4. Ajmal, S.; Athar Hashmi, F.; Imran, I. Recent Progress in Development and Applications of Biomaterials. *Materials Today: Proceedings* **2022**, *62*, 385–391, doi:10.1016/j.matpr.2022.04.233.
5. Liu, X.; Ma, P.X. Polymeric Scaffolds for Bone Tissue Engineering. *Annals of Biomedical Engineering* **2004**, *32*, 477–486, doi:10.1023/b:abme.0000017544.36001.8e.
6. Deshmukh, K.; Kovářík, T.; Křenek, T.; Docheva, D.; Stich, T.; Pola, J. Recent Advances and Future Perspectives of Sol–Gel Derived Porous Bioactive Glasses: A Review. *RSC Adv.* **2020**, *10*, 33782–33835, doi:10.1039/d0ra04287k.
7. Vijayakumar, N.; Venkatraman, S.K.; Soundhariyaa, T.N.; Mohan, S.; Magesvaran, M.K.; Genasan, K.; Alex, R.A.; Abraham, J.; Swamiappan, S. FUEL-ASSISTED SOL-GEL COMBUSTION SYNTHESIS OF MONTICELLITE: STRUCTURAL, MECHANICAL, AND BIOLOGICAL CHARACTERIZATION FOR TISSUE ENGINEERING. *Journal of Science: Advanced Materials and Devices* **2025**, 100951, doi:10.1016/j.jsamd.2025.100951.
8. Thapa, R.K.; Kiick, K.L.; Sullivan, M.O. Encapsulation of Collagen Mimetic Peptide-Tethered Vancomycin Liposomes in Collagen-Based Scaffolds for Infection Control in Wounds. *Acta Biomaterialia* **2020**, *103*, 115–128, doi:10.1016/j.actbio.2019.12.014.
9. D'Angelo, A.; Fiorentino, M.; Viola, V.; Vertuccio, L.; Catauro, M. Effect of Nitric Acid on the Synthesis and Biological Activity of Silica–Quercetin Hybrid Materials via the Sol-Gel Route. *Applied Sciences* **2024**, *14*, 5268, doi:10.3390/app14125268.
10. Shoushtari, M.S.; Hoey, D.; Biak, D.R.A.; Abdullah, N.; Kamarudin, S.; Zainuddin, H.S. Sol–Gel-templated Bioactive Glass Scaffold: A Review. *Res. Biomed. Eng.* **2024**, *40*, 281–296, doi:10.1007/s42600-024-00342-x.
11. Niari, S.A.; Rahbarghazi, R.; Geranmayeh, M.H.; Karimipour, M. Biomaterials Patterning Regulates Neural Stem Cells Fate and Behavior: The Interface of Biology and Material Science. *J Biomedical Materials Res* **2022**, *110*, 725–737, doi:10.1002/jbm.a.37321.
12. Raffaini, G.; Pirozzi, P.; Catauro, M.; D'Angelo, A. Hybrid Organic–Inorganic Biomaterials as Drug Delivery Systems: A Molecular Dynamics Study of Quercetin Adsorption on Amorphous Silica Surfaces. *Coatings* **2024**, *14*, 234, doi:10.3390/coatings14020234.
13. Pamula, E.; Kokoszka, J.; Cholewa-Kowalska, K.; Laczka, M.; Kantor, L.; Niedzwiedzki, L.; Reilly, G.C.; Filipowska, J.; Madej, W.; Kolodziejczyk, M.; et al. Degradation, Bioactivity, and Osteogenic Potential of Composites Made of PLGA and Two Different Sol–Gel Bioactive Glasses. *Ann Biomed Eng* **2011**, *39*, 2114–2129, doi:10.1007/s10439-011-0307-4.
14. Zdarta, J.; Jesionowski, T. Silica and Silica-Based Materials for Biotechnology, Polymer Composites, and Environmental Protection. *Materials* **2022**, *15*, 7703, doi:10.3390/ma15217703.
15. Dixit, M.; Mishra, M.; Joshi, P.A.; Shah, D.O. Study on the Catalytic Properties of Silica Supported Copper Catalysts. *Procedia Engineering* **2013**, *51*, 467–472, doi:10.1016/j.proeng.2013.01.066.

16. Azizi, L.; Turkki, P.; Huynh, N.; Massera, J.M.; Hytönen, V.P. Surface Modification of Bioactive Glass Promotes Cell Attachment and Spreading. *ACS Omega* **2021**, *6*, 22635–22642, doi:10.1021/acsomega.1c02669.
17. Sodium Alginate in Drug Delivery and Biomedical Areas. In *Natural Polysaccharides in Drug Delivery and Biomedical Applications*; Elsevier, 2019; pp. 59–100 ISBN 978-0-12-817055-7.
18. Ahmad Raus, R.; Wan Nawawi, W.M.F.; Nasaruddin, R.R. Alginate and Alginate Composites for Biomedical Applications. *Asian Journal of Pharmaceutical Sciences* **2021**, *16*, 280–306, doi:10.1016/j.ajps.2020.10.001.
19. Shah, F.A.; Thomsen, P.; Palmquist, A. Osseointegration and Current Interpretations of the Bone-Implant Interface. *Acta Biomaterialia* **2019**, *84*, 1–15, doi:10.1016/j.actbio.2018.11.018.
20. Drago, E.; Campardelli, R.; Pettinato, M.; Perego, P. Innovations in Smart Packaging Concepts for Food: An Extensive Review. *Foods* **2020**, *9*, 1628, doi:10.3390/foods9111628.
21. De Paula, J.H.; Quevedo, B.V.; Komatsu, D.; Santos, A.R.; De Souza, A.L.; De Rezende Duek, E.A. Development of Silica/Collagen Hybrids Synthesized Via a Simplified Sol-Gel Reaction for Biomaterial Applications. *Silicon* **2025**, *17*, 1693–1705, doi:10.1007/s12633-025-03302-x.
22. Maleki, H.; Shahbazi, M.-A.; Montes, S.; Hosseini, S.H.; Eskandari, M.R.; Zaunschirm, S.; Verwanger, T.; Mathur, S.; Milow, B.; Krammer, B.; et al. Mechanically Strong Silica-Silk Fibroin Bioaerogel: A Hybrid Scaffold with Ordered Honeycomb Micromorphology and Multiscale Porosity for Bone Regeneration. *ACS Appl. Mater. Interfaces* **2019**, *11*, 17256–17269, doi:10.1021/acsami.9b04283.
23. Abka-khajouei, R.; Tounsi, L.; Shahabi, N.; Patel, A.K.; Abdelkafi, S.; Michaud, P. Structures, Properties and Applications of Alginates. *Marine Drugs* **2022**, *20*, 364, doi:10.3390/md20060364.
24. Guo, X.; Wang, Y.; Qin, Y.; Shen, P.; Peng, Q. Structures, Properties and Application of Alginic Acid: A Review. *International Journal of Biological Macromolecules* **2020**, *162*, 618–628, doi:10.1016/j.ijbiomac.2020.06.180.
25. Zhang, X.; Huang, C.; Zhao, Y.; Jin, X. Preparation and Characterization of Nanoparticle Reinforced Alginate Fibers with High Porosity for Potential Wound Dressing Application. *RSC Adv.* **2017**, *7*, 39349–39358, doi:10.1039/c7ra06103j.
26. Abdelhamid, M.A.A.; Khalifa, H.O.; Ki, M.-R.; Pack, S.P. Nanoengineered Silica-Based Biomaterials for Regenerative Medicine. *IJMS* **2024**, *25*, 6125, doi:10.3390/ijms25116125.
27. Lee, Y.-G.; Park, J.-H.; Oh, C.; Oh, S.-G.; Kim, Y.C. Preparation of Highly Monodispersed Hybrid Silica Spheres Using a One-Step Sol−Gel Reaction in Aqueous Solution. *Langmuir* **2007**, *23*, 10875–10878, doi:10.1021/la702462b.
28. Marangoni Júnior, L.; Da Silva, R.G.; Anjos, C.A.R.; Vieira, R.P.; Alves, R.M.V. Effect of Low Concentrations of SiO2 Nanoparticles on the Physical and Chemical Properties of Sodium Alginate-Based Films. *Carbohydrate Polymers* **2021**, *269*, 118286, doi:10.1016/j.carbpol.2021.118286.
29. Marangoni Júnior, L.; Fozzatti, C.R.; Jamróz, E.; Vieira, R.P.; Alves, R.M.V. Biopolymer-Based Films from Sodium Alginate and Citrus Pectin Reinforced with SiO2. *Materials* **2022**, *15*, 3881, doi:10.3390/ma15113881.
30. Ashour, M.M.; Mabrouk, M.; Soliman, I.E.; Beherei, H.H.; Tohamy, K.M. Mesoporous Silica Nanoparticles Prepared by Different Methods for Biomedical Applications: Comparative Study. *IET Nanobiotechnology* **2021**, *15*, 291–300, doi:10.1049/nbt2.12023.
31. Thakur, S.; Arotiba, O.A. Synthesis, Swelling and Adsorption Studies of a pH-Responsive Sodium Alginate–Poly(Acrylic Acid) Superabsorbent Hydrogel. *Polym. Bull.* **2018**, *75*, 4587–4606, doi:10.1007/s00289-018-2287-0.
32. Dalal, S.R.; Hussein, M.H.; El-Naggar, N.E.-A.; Mostafa, S.I.; Shaaban-Dessuuki, S.A. Characterization of Alginate Extracted from Sargassum Latifolium and Its Use in Chlorella Vulgaris Growth Promotion and Riboflavin Drug Delivery. *Sci Rep* **2021**, *11*, doi:10.1038/s41598-021-96202-0.
33. Salisu, A.; Sanagi, M.M.; Abu Naim, A.; Abd Karim, K.J.; Wan Ibrahim, W.A.; Abdulganiyu, U. Alginate Graft Polyacrylonitrile Beads for the Removal of Lead from Aqueous Solutions. *Polym. Bull.* **2016**, *73*, 519–537, doi:10.1007/s00289-015-1504-3.
34. Onbas, R.; Yesil-Celiktas, O. Synthesis of Alginate-silica Hybrid Hydrogel for Biocatalytic Conversion by Β-glucosidase in Microreactor. *Engineering in Life Sciences* **2019**, *19*, 37–46, doi:10.1002/elsc.201800124.

35. Tabish, M.S.; Hanapi, N.S.M.; Ibrahim, W.N.W.; Saim, N.; Yahaya, N. Alginate-Graphene Oxide Biocomposite Sorbent for Rapid and Selective Extraction of Non-Steroidal Anti-Inflammatory Drugs Using Micro-Solid Phase Extraction. *Indones. J. Chem.* **2019**, *19*, 684, doi:10.22146/ijc.38168.
36. Derkach, S.R.; Voron'ko, N.G.; Sokolan, N.I.; Kolotova, D.S.; Kuchina, Y.A. Interactions between Gelatin and Sodium Alginate: UV and FTIR Studies. *Journal of Dispersion Science and Technology* **2020**, *41*, 690–698, doi:10.1080/01932691.2019.1611437.
37. Pannier, A.; Soltmann, U.; Soltmann, B.; Altenburger, R.; Schmitt-Jansen, M. Alginate/Silica Hybrid Materials for Immobilization of Green Microalgae Chlorella Vulgaris for Cell-Based Sensor Arrays. *J. Mater. Chem. B* **2014**, *2*, 7896–7909, doi:10.1039/c4tb00944d.
38. Fiorentino, M.; Piccolella, S.; Gravina, C.; Stinca, A.; Esposito, A.; Catauro, M.; Pacifico, S. Encapsulating Calendula Arvensis (Vaill.) L. Florets: UHPLC-HRMS Insights into Bioactive Compounds Preservation and Oral Bioaccessibility. *Molecules* **2022**, *28*, 199, doi:10.3390/molecules28010199.
39. Kebede, G.G.; Mitev, P.D.; Briels, W.J.; Hermansson, K. Red-Shifting and Blue-Shifting OH Groups on Metal Oxide Surfaces – towards a Unified Picture. *Phys. Chem. Chem. Phys.* **2018**, *20*, 12678–12687, doi:10.1039/c8cp00741a.
40. Jiang, X.; Tang, X.; Tang, L.; Zhang, B.; Mao, H. Synthesis and Formation Mechanism of Amorphous Silica Particles via Sol–Gel Process with Tetraethylorthosilicate. *Ceramics International* **2019**, *45*, 7673–7680, doi:10.1016/j.ceramint.2019.01.067.
41. De Los Arcos, T.; Müller, H.; Wang, F.; Damerla, V.R.; Hoppe, C.; Weinberger, C.; Tiemann, M.; Grundmeier, G. Review of Infrared Spectroscopy Techniques for the Determination of Internal Structure in Thin SiO2 Films. *Vibrational Spectroscopy* **2021**, *114*, 103256, doi:10.1016/j.vibspec.2021.103256.
42. Wiercigroch, E.; Szafraniec, E.; Czamara, K.; Pacia, M.Z.; Majzner, K.; Kochan, K.; Kaczor, A.; Baranska, M.; Malek, K. Raman and Infrared Spectroscopy of Carbohydrates: A Review. *Spectrochimica Acta Part A: Molecular and Biomolecular Spectroscopy* **2017**, *185*, 317–335, doi:10.1016/j.saa.2017.05.045.
43. Villacrés, N.A.; Cavalheiro, E.; Schmitt, C.; Venâncio, T.; Alarcón, H.; Valderrama, A. Preparation of Composite Films of Sodium Alginate-Based Extracted from Seaweeds Macrocystis Pyrifera and Lessonia Trabeculata Loaded with Aminoethoxyvinylglycine. *J. Braz. Chem. Soc.* **2023**, doi:10.21577/0103-5053.20230064.
44. Jyoti Borah, S.; Kumar, R.; Prasad Singh, P.; Kumar, V. SnO_2 Encapsulated in Alginate Matrix: Evaluation and Optimization of Bioinspired Nanoadsorbents for Azo Dye Removal. *ChemBioChem* **2024**, *25*, doi:10.1002/cbic.202400567.
45. Sundarrajan, P.; Eswaran, P.; Marimuthu, A.; Subhadra, L.B.; Kannaiyan, P. One Pot Synthesis and Characterization of Alginate Stabilized Semiconductor Nanoparticles. *Bulletin of the Korean Chemical Society* **2012**, *33*, 3218–3224, doi:10.5012/BKCS.2012.33.10.3218.
46. Mortalò, C.; Russo, P.; Miorin, E.; Zin, V.; Paradisi, E.; Leonelli, C. Extruded Composite Films Based on Polylactic Acid and Sodium Alginate. *Polymer* **2023**, *282*, 126162, doi:10.1016/j.polymer.2023.126162.
47. Paradisi, E.; Mortalò, C.; Russo, P.; Zin, V.; Miorin, E.; Montagner, F.; Leonelli, C.; Deambrois, S.M. Facile and Effective Method for the Preparation of Sodium Alginate/TiO_2 Bio-Composite Films for Different Applications. *Macromolecular Symposia* **2024**, *413*, doi:10.1002/masy.202300230.
48. Skwira, A.; Szewczyk, A.; Konopacka, A.; Górska, M.; Majda, D.; Sądej, R.; Prokopowicz, M. Silica-Polymer Composites as the Novel Antibiotic Delivery Systems for Bone Tissue Infection. *Pharmaceutics* **2019**, *12*, 28, doi:10.3390/pharmaceutics12010028.
49. Ebnalwaled, A.A.; Sadek, A.H.; Ismail, S.H.; Mohamed, G.G. Structural, Optical, Dielectric, and Surface Properties of Polyimide Hybrid Nanocomposites Films Embedded Mesoporous Silica Nanoparticles Synthesized from Rice Husk Ash for Optoelectronic Applications. *Opt Quant Electron* **2022**, *54*, doi:10.1007/s11082-022-03976-2.
50. Han, X.; Liang, J.; Fukuda, S.; Zhu, L.; Wang, S. Sodium Alginate–Silica Composite Aerogels from Rice Husk Ash for Efficient Absorption of Organic Pollutants. *Biomass and Bioenergy* **2022**, *159*, 106424, doi:10.1016/j.biombioe.2022.106424.

51. Qi, Y.; Li, J.; Chen, Y.; Zhu, B.; Zhou, X.; Xiao, X.; Gu, Z.; Qian, J.; He, C.; Lai, M.; et al. Differential Fiber Optic Humidity Sensor Based on Superhydrophilic SiO2/Polyethylene Glycol Composite Film with Linear Response. *Optical Fiber Technology* **2025**, *90*, 104150, doi:10.1016/j.yofte.2025.104150.
52. Zhang, D.; Ding, J.; Zhou, Y.; Ju, J. Research Progress on Moisture-Sorption Actuators Materials. *Nanomaterials* **2024**, *14*, 1544, doi:10.3390/nano14191544.
53. Gómez Vargas, C.; Ponce, N.M.A.; Stortz, C.A.; Fissore, E.N.; Bonelli, P.; Otálora González, C.M.; Gerschenson, L.N. Pectin Obtention from Agroindustrial Wastes of Malus Domestica Using Green Solvents (Citric Acid and Natural Deep Eutectic Solvents). Chemical, Thermal, and Rheological Characterization. *Front. Chem.* **2025**, *12*, doi:10.3389/fchem.2024.1504582.
54. Akshaya, S.; Nathanael, A.J. A Review on Hydrophobically Associated Alginates: Approaches and Applications. *ACS Omega* **2024**, *9*, 4246–4262, doi:10.1021/acsomega.3c08619.
55. Hernández-González, A.C.; Téllez-Jurado, L.; Rodríguez-Lorenzo, L.M. Preparation of Covalently Bonded Silica-Alginate Hybrid Hydrogels by SCHIFF Base and Sol-Gel Reactions. *Carbohydrate Polymers* **2021**, *267*, 118186, doi:10.1016/j.carbpol.2021.118186.
56. Flores-Hernández, C.G.; Cornejo-Villegas, M.D.L.A.; Moreno-Martell, A.; Del Real, A. Synthesis of a Biodegradable Polymer of Poly (Sodium Alginate/Ethyl Acrylate). *Polymers* **2021**, *13*, 504, doi:10.3390/polym13040504.
57. Dos Santos Araújo, P.; Belini, G.B.; Mambrini, G.P.; Yamaji, F.M.; Waldman, W.R. Thermal Degradation of Calcium and Sodium Alginate: A Greener Synthesis towards Calcium Oxide Micro/Nanoparticles. *International Journal of Biological Macromolecules* **2019**, *140*, 749–760, doi:10.1016/j.ijbiomac.2019.08.103.
58. Liu, L.; Lu, Y.; Qiu, D.; Wang, D.; Ding, Y.; Wang, G.; Liang, Z.; Shen, Z.; Li, A.; Chen, X.; et al. Sodium Alginate-Derived Porous Carbon: Self-Template Carbonization Mechanism and Application in Capacitive Energy Storage. *Journal of Colloid and Interface Science* **2022**, *620*, 284–292, doi:10.1016/j.jcis.2022.04.022.
59. Soares, J.D.P.; Dos Santos, J.E.; Chierice, G.O.; Cavalheiro, É.T.G. Thermal Behavior of Alginic Acid and Its Sodium Salt. *Eclet. Quim.* **2004**, *29*, 57–63, doi:10.26850/1678-4618eqj.v29.2.2004.p57-63.
60. Wei, J.; Yang, S.; Zhu, Z.; Lu, J.; Zhang, B.; Zhang, M.; Wei, W. Low-Temperature Dried Alginate/Silica Hybrid Aerogel Beads with Tunable Surface Functionalities for Removal of Lead Ions from Water. *Gels* **2025**, *11*, 397, doi:10.3390/gels11060397.
61. Fernando, I.P.S.; Jayawardena, T.U.; Sanjeewa, K.K.A.; Wang, L.; Jeon, Y.-J.; Lee, W.W. Anti-Inflammatory Potential of Alginic Acid from Sargassum Horneri against Urban Aerosol-Induced Inflammatory Responses in Keratinocytes and Macrophages. *Ecotoxicology and Environmental Safety* **2018**, *160*, 24–31, doi:10.1016/j.ecoenv.2018.05.024.
62. Spyrogianni, A.; Sotiriou, G.A.; Brambilla, D.; Leroux, J.-C.; Pratsinis, S.E. The Effect of Settling on Cytotoxicity Evaluation of SiO2 Nanoparticles. *Journal of Aerosol Science* **2017**, *108*, 56–66, doi:10.1016/j.jaerosci.2017.02.011.
63. Fiorentino, M.; D'Angelo, A.; Vertuccio, L.; Khan, H.; Catauro, M. Characterization of Grape Extract-Colored SiO2 Synthesized via the Sol–Gel Method. *Applied Sciences* **2024**, *14*, 11697, doi:10.3390/app142411697.
64. Piccolella, S.; Fiorentino, M.; Cimmino, G.; Esposito, A.; Pacifico, S. Cilentan Cichorium Intybus L. Organs: UHPLC-QqTOF-MS/MS Analysis for New Antioxidant Scenario, Exploitable Locally and Beyond. *Future Foods* **2024**, *9*, 100379, doi:10.1016/j.fufo.2024.100379.
65. Brahmi-Chendouh, N.; Piccolella, S.; Gravina, C.; Fiorentino, M.; Formato, M.; Kheyar, N.; Pacifico, S. Ready-to-Use Nutraceutical Formulations from Edible and Waste Organs of Algerian Artichokes. *Foods* **2022**, *11*, 3955, doi:10.3390/foods11243955.